

# Large electrostrictive response in lead halide perovskites

Bo Chen<sup>1,6</sup>, Tao Li<sup>2,6</sup>, Qingfeng Dong<sup>1</sup>, Edoardo Mosconi<sup>3,4</sup>, Jingfeng Song<sup>1,2</sup>, Zhaolai Chen<sup>1</sup>, Yehao Deng<sup>1</sup>, Ye Liu<sup>1</sup>, Stephen Ducharme<sup>1,2</sup>, Alexei Gruverman<sup>1,2</sup>, Filippo De Angelis<sup>3,4\*</sup> and Jinsong Huang<sup>1,5\*</sup>

**Lead halide perovskites have demonstrated outstanding performance in photovoltaics, photodetectors, radiation detectors and light-emitting diodes. However, the electromechanical properties, which are the main application of inorganic perovskites, have rarely been explored for lead halide perovskites. Here, we report the discovery of a large electrostrictive response in methylammonium lead triiodide (MAPbI<sub>3</sub>) single crystals. Under an electric field of 3.7 V μm<sup>-1</sup>, MAPbI<sub>3</sub> shows a large compressive strain of 1%, corresponding to a mechanical energy density of 0.74 J cm<sup>-3</sup>, comparable to that of human muscles. The influences of piezoelectricity, thermal expansion, intrinsic electrostrictive effect, Maxwell stress, ferroelectricity, local polar fluctuation and methylammonium cation ordering on this electromechanical response are excluded. We speculate, using density functional theory, that electrostriction of MAPbI<sub>3</sub> probably originates from lattice deformation due to formation of additional defects under applied bias. The discovery of large electrostriction in lead iodide perovskites may lead to new potential applications in actuators, sonar and micro-electromechanical systems and aid the understanding of other field-dependent material properties.**

Organic–inorganic hybrid perovskites (OIHPs) have attracted extensive interest for potential use in next-generation photovoltaic devices due to the demonstrated high power conversion efficiency, low materials cost and low fabrication cost<sup>1,2</sup>. OIHP materials display extraordinary optoelectronic properties, such as a large absorption coefficient, high carrier mobility and long carrier recombination lifetimes, which benefit their outstanding performance in solar cells, photodetectors, X-ray detectors, γ-ray detectors and light-emitting diodes (LEDs)<sup>3–9</sup>. Solar cells based on OIHP thin films have achieved a certified power conversion efficiency of 23.3%<sup>2</sup>. OIHP photodetectors based on MAPbI<sub>3</sub> thin films demonstrate high specific detectivity, a low detection limit of 0.64 pW cm<sup>-2</sup> and ultrafast sub-nanosecond response time<sup>3,4</sup>. The strong surface-charge recombination enables a unique narrow spectral response with full-width at half-maximum of less than 20 nm in OIHP single-crystal photodetectors<sup>5</sup>. Due to the high mobility–lifetime product ( $\mu\tau$ ) and large atomic number, MAPbBr<sub>3</sub> single-crystal X-ray detectors have shown a high sensitivity of  $2.1 \times 10^4 \mu\text{C Gy}_{\text{air}}^{-1} \text{cm}^{-2}$  under 8 keV X-ray radiation, which is over a thousand times better than commercial amorphous selenium X-ray detectors<sup>6</sup>. The dopant-compensated MAPbBr<sub>2.94</sub>Cl<sub>0.06</sub> single crystals have dramatically reduced the free carrier concentration and increased the carrier mobility, yielding an outstanding γ-ray spectrometer with a resolution comparable to that of a standard scintillator γ-ray detector<sup>7</sup>. OIHP LEDs have demonstrated tunable emission wavelengths, a maximum external quantum efficiency of 10.4% and the largest peak luminance of 20,000 cd m<sup>-2</sup><sup>8,9</sup>.

For conventional inorganic perovskites, commercial applications mainly rely on the strong electromechanical coupling, including both piezoelectricity and electrostriction. The direct

piezoelectric effect converts mechanical energy into electrical energy, with applications in piezoelectric sensors and piezoelectric generators<sup>10</sup>. For example, a sonar system based on piezoelectric sensors could transmit and receive ultrasonic signals for underwater communication. Piezoelectric generators have been used for ignition in lighters and also to harvest mechanical energy at both macroscopic scales and nanoscales<sup>11</sup>. The inverse piezoelectric effect creates material deformation under an applied electric field, which enables many applications of piezoelectric actuators, such as accurate position controllers for optical cameras and telescopes, and ultrasound generation for ultrasonic cleaning systems and sonars<sup>12</sup>. Electrostriction is an electromechanical coupling with strain proportional to the square of applied electric field, while piezoelectric strain is linear with applied electric field. Two types of electrostrictive material have been explored, including relaxor ferroelectric ceramics and electrostrictive polymers<sup>13–27</sup>. Electrostriction can allow a material to achieve larger strain at high applied fields than does piezoelectricity. The piezoelectric strain is typically of the order of 0.1%, while electrostrictive materials can achieve a strain of 5% or more<sup>13–27</sup>.

OIHPs possess a similar lattice structure to conventional inorganic perovskites; however, the electromechanical coupling of OIHPs has barely been explored. Here, we report the observation of a strong electromechanical response of MAPbI<sub>3</sub> single crystals. The measured electromechanical strain is proportional to the square of electric field, which indicates an electrostrictive property of MAPbI<sub>3</sub>. It has been found that the MAPbI<sub>3</sub> single crystal exhibits a compressive strain of up to 1% with a mechanical energy density of 0.74 J cm<sup>-3</sup>, which is higher than that of most existing electrostrictive materials.

<sup>1</sup>Department of Mechanical and Materials Engineering, University of Nebraska-Lincoln, Lincoln, NE, USA. <sup>2</sup>Department of Physics and Astronomy, and Nebraska Center for Materials and Nanoscience, University of Nebraska-Lincoln, Lincoln, NE, USA. <sup>3</sup>Computational Laboratory for Hybrid/Organic Photovoltaics (CLHYO), CNR-ISTM, Perugia, Italy. <sup>4</sup>D3-Computation, Istituto Italiano di Tecnologia, Genova, Italy. <sup>5</sup>Department of Applied Physical Sciences, University of North Carolina, Chapel Hill, NC, USA. <sup>6</sup>These authors contributed equally: Bo Chen, Tao Li. \*e-mail: [filippo@thch.unipg.it](mailto:filippo@thch.unipg.it); [jhuang@unc.edu](mailto:jhuang@unc.edu)

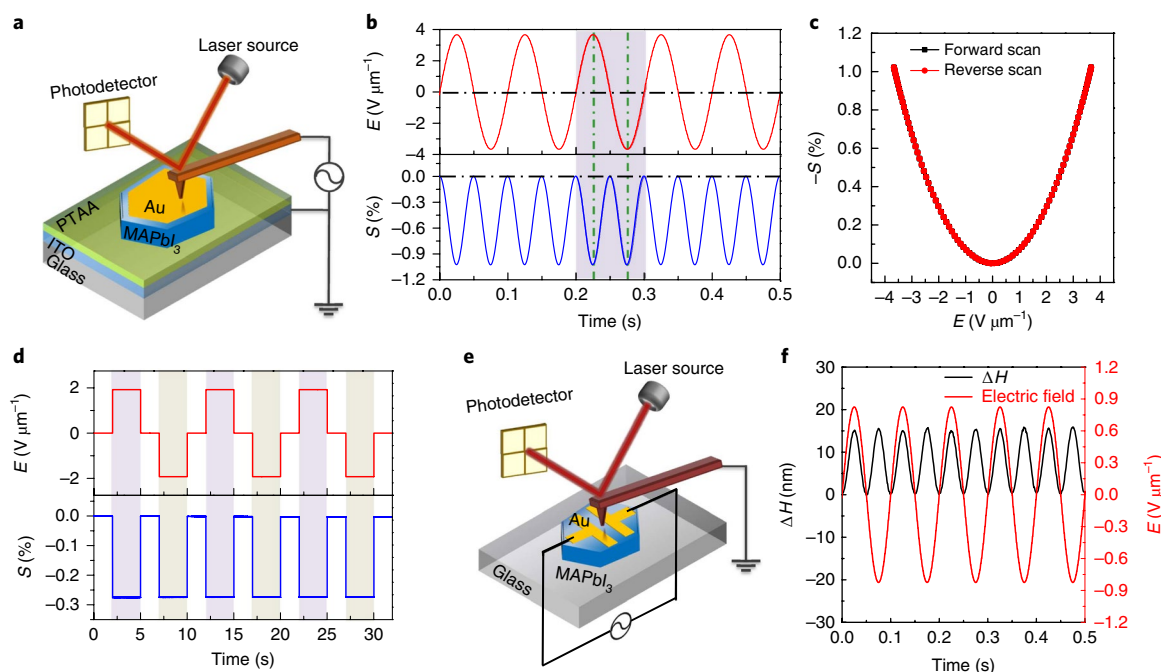


**Fig. 1 | Electrostrictive response of MAPbI<sub>3</sub> single crystal.** **a**, Schematic illustration of AFM measurement of strain induced by electric field. **b**, Electrostrictive strain of a 40  $\mu\text{m}$  MAPbI<sub>3</sub> single crystal under a.c. bias at 10 Hz. **c**, Relation between strain and electric field for the MAPbI<sub>3</sub> single crystal in **b**. **d**, Electrostrictive strain under alternating electric fields of 0, 1.9, 0, and  $-1.9 \text{ V } \mu\text{m}^{-1}$ . **e, f**, Schematic illustration of setup (**e**) and experimental result (**f**) for out-of-plane lattice deformation under in-plane electric field.  $\Delta H$  is the detected thickness change by AFM.

### High electrostriction in MAPbI<sub>3</sub>

We detected a high strain induced by electric field in MAPbI<sub>3</sub> single crystals under a field of less than  $10 \text{ V } \mu\text{m}^{-1}$  by atomic force microscopy (AFM) measurement (Fig. 1). MAPbI<sub>3</sub> single crystals with thickness of  $40 \mu\text{m}$  were grown directly on a poly(bis(4-phenyl)(2,4,6-trimethylphenyl)amine)- (PTAA-) coated indium tin oxide (ITO)-glass substrate using a non-wetting surface-induced space-confined method<sup>28</sup>. Under an a.c. electric field of  $3.7 \text{ V } \mu\text{m}^{-1}$  with a frequency of 10 Hz, the MAPbI<sub>3</sub> single crystal shows thickness oscillation with the maximum amplitude corresponding to 1% strain (Fig. 1b). It is noted that MAPbI<sub>3</sub> single crystals contract under both positive and negative bias irrespective of the field polarity, which is also confirmed with a d.c. bias pulse in Fig. 1d. As a result, the frequency of the strain induced by electric field is twice the applied a.c. bias. The magnitude of field-induced strain could be easily tuned by changing the amplitude of the a.c. bias (Supplementary Fig. 1). We measured the magnitude of strain under different fields. As shown in Fig. 1c, the strain ( $S$ ) and electric field ( $E$ ) showed a quadratic relationship:

$$S = M \times E^2 \quad (1)$$

where  $M$  is the electrostrictive coefficient. This quadratic relationship indicates that the electromechanical response here is dominated by electrostriction. The calculated electrostrictive coefficient is  $-730 \text{ nm}^2 \text{ V}^{-2}$  for MAPbI<sub>3</sub> single crystals, which is the largest among all reported electrostrictive materials, with details summarized in Table 1. For the most popular electrostrictive ceramic,  $\text{Pb}(\text{Zn}_{1/3}\text{Nb}_{2/3})\text{O}_3$ -8%  $\text{PbTiO}_3$ , and electrostrictive polymer,  $\text{P}(\text{VDF-TrFE})/\text{CuPc}$ , the electrostrictive coefficient is  $120 \text{ nm}^2 \text{ V}^{-2}$  and  $-113 \text{ nm}^2 \text{ V}^{-2}$ , respectively<sup>16,24</sup>. The large electrostrictive response allows observation of material shape change with the naked eye (Supplementary Video 1). Supplementary Video 1 also shows that some strip lines appeared on the surfaces of a MAPbI<sub>3</sub> crystal under applied pulse bias<sup>29</sup>, which can be

explained by twin formation under the high electrostrictive strain induced by the applied field. Twin structures have been previously observed in both single-crystalline and polycrystalline MAPbI<sub>3</sub> due to the ferroelastic properties of this material<sup>30</sup>.

Superior to other electrostrictive materials, MAPbI<sub>3</sub> demonstrates both high electrostrictive strain and large elastic energy densities under a small applied field (as shown in Table 1). However, for other electrostrictive materials, tens or even thousands of volts per micrometre are required to achieve comparable electrostrictive strain or elastic energy density. The electrostrictive strain for relaxor ferroelectric ceramics is of the order of 0.1%<sup>13-20</sup>. Electrostrictive polymers display electrostrictive strain exceeding 5% with elastic energy density of the order of  $0.1 \text{ J cm}^{-3}$ ; however, the electrostrictive polymers require high operation field of more than  $100 \text{ V } \mu\text{m}^{-1}$ <sup>21-23</sup>. Raising the polarization density by introducing materials with high dielectric constant into a  $\text{P}(\text{VDF-TrFE})$  matrix to form electrostrictive polymer composites can reduce the electric field needed to approach 5% strain to tens of volts per micrometre, while their low Young's modulus ( $<1 \text{ GPa}$ ) limits the elastic energy densities less than  $0.5 \text{ J cm}^{-3}$ <sup>24-27</sup>. Although the electrostrictive strain of MAPbI<sub>3</sub> is only 1%, its large electrostrictive coefficient and relatively large Young's modulus of  $14.8 \text{ GPa}$  (Supplementary Fig. 2) enable MAPbI<sub>3</sub> single crystals to achieve a record high mechanical energy density of  $0.74 \text{ J cm}^{-3}$  under an applied electric field of only  $3.7 \text{ V } \mu\text{m}^{-1}$ . This mechanical energy density is comparable to that of human muscles, and on a par with typical actuator materials ( $0.016$  to  $1.0 \text{ J cm}^{-3}$ )<sup>31-34</sup>.

The contraction of perovskite crystals along the direction of the applied field may be accompanied by expansion of the crystal lattice in the direction perpendicular to the applied electric field, which is determined by the components of the piezoelectric and electrostriction tensors. In order to measure it, we fabricated lateral-structure devices with two Au electrodes on the top surface of MAPbI<sub>3</sub> single crystals, as illustrated in Fig. 1e. The in-plane electric field was applied in parallel with the crystal surface, while the crystal thickness

**Table 1 | Comparison of electrostrictive response of relaxor ferroelectric ceramic, electrostrictive polymers and MAPbI<sub>3</sub> hybrid perovskite**

Type	Materials	S <sub>m</sub> (%)	Y (GPa)	YS <sub>m</sub> <sup>2</sup> /2 (J cm <sup>-3</sup> )	E <sub>m</sub> (V μm <sup>-1</sup> )	M (nm <sup>2</sup> V <sup>-2</sup> )	Ref.
Relaxor ferroelectric ceramic	Pb(Zn <sub>1/3</sub> Nb <sub>2/3</sub> )O <sub>3</sub> -8% PbTiO <sub>3</sub>	1.7	7.7	1.11	12	120	16,21
	Pb(Zn <sub>1/3</sub> Nb <sub>2/3</sub> )O <sub>3</sub>	0.44	—	—	8	69	17
	Pb(Mg <sub>1/3</sub> Nb <sub>2/3</sub> )O <sub>3</sub> -0.27 PbTiO <sub>3</sub>	0.34	115	0.66	10	34	18,19
	Pb(Mg <sub>1/3</sub> Nb <sub>2/3</sub> )O <sub>3</sub>	0.13	—	—	8	20	20
	K <sub>0.5</sub> Na <sub>0.5</sub> NbO <sub>3</sub> -SrTiO <sub>3</sub>	0.006	—	—	2	15	13
	Bi <sub>0.5</sub> Na <sub>0.5</sub> TiO <sub>3</sub> -BaTiO <sub>3</sub> -KNbO <sub>3</sub>	0.11	—	—	4	69	14
	5% Sn-doped Bi <sub>1/2</sub> (Na <sub>0.82</sub> K <sub>0.18</sub> ) <sub>1/2</sub> TiO <sub>3</sub>	0.32	—	—	6	90	13
	2% Fe-doped Ba(Zr <sub>0.2</sub> Ti <sub>0.8</sub> )O <sub>3</sub> -0.5(Ba <sub>0.7</sub> Ca <sub>0.3</sub> )TiO <sub>3</sub>	0.14	—	—	3	156	15
Electrostrictive polymer	Irradiated P(VDF-TrFE)	-4	0.38	0.30	150	-1.8	21
	P(VDF-TrFE-CTFE)	-4	0.4	0.32	150	-1.8	22
	P(VDF-TrFE-CFE)	-7	0.3	0.73	165	-2.6	23
	P(VDF-TrFE)/CuPc	-1.91	0.75	0.14	13	-113	24
	P(VDF-TrFE-CTFE)/polyaniline	-2.65	0.53	0.19	16	-104	25
	P(VDF-TrFE-CFE)/graphene	-4.1	0.56	0.47	23	-78	26
	P(VDF-TrFE-CFE)/DEHP	-1.8	0.04	0.01	10	-180	27
Hybrid perovskites	MAPbI <sub>3</sub>	-1	14.8	0.74	3.7	-730	This work

S<sub>m</sub> is the maximum strain response, Y is Young's modulus, YS<sub>m</sub><sup>2</sup>/2 is the mechanical energy density, E<sub>m</sub> is the required applied electric field for S<sub>m</sub> and M is the electrostrictive coefficient.

change along the out-of-plane direction was monitored by the AFM tip. We found that the MAPbI<sub>3</sub> single crystal expands along the out-of-plane direction (Fig. 1f).

### Macroscopic measurement of electrostrictive response

The macroscopic strain of the crystals was measured directly with laser interferometry to verify the strain in the perovskite crystals under bias. The geometry of measurement is shown in Fig. 2a. It is worth pointing out that both piezoelectric effect and electrostriction can cause an electromechanical response, while they can be distinguished by their different field-dependent strain relationships (Supplementary Section 1.0). Piezoelectricity is a first-order electromechanical coupling where the strain is proportional to the electric field, while electrostriction is second-order coupling in which the strain is proportional to the square of the electric field. Here we measured the strain dependent on electric field at 100 Hz. The frequency of 100 Hz was chosen to obtain a large signal-to-noise ratio and thus a reliable reading in the piezoelectric response. As shown in Fig. 2b, the MAPbI<sub>3</sub> single crystal shows both piezoelectric and electrostrictive responses. The electrostrictive response is one order of magnitude stronger than the piezoelectric response (Fig. 2b). The first-order piezoelectric response is small, with a piezoelectric coefficient (*d*<sub>33</sub>) of 3.1 pm V<sup>-1</sup>. This *d*<sub>33</sub> value is very close to a previously measured value of 2.7 pm V<sup>-1</sup> at a higher frequency of 1 kHz<sup>29</sup>, and in excellent agreement with the value calculated in ref. 35. The occurrence of a high electrostrictive strain should be detected by X-ray diffraction (XRD). Figure 2c shows the geometry of XRD characterization of a MAPbI<sub>3</sub> single crystal under an electric field of 2.5 V μm<sup>-1</sup>. As shown in Fig. 2d, a shift of the XRD peak for the (200) plane to a larger diffraction angle is indeed observed when the MAPbI<sub>3</sub> single crystal is under an applied field along the out-of-plane direction, which confirms the contraction of the lattice along the field direction. The XRD peak shift direction is opposite to that caused by the thermal expansion, because thermal expansion of the MAPbI<sub>3</sub> single crystal should shift the XRD peaks to smaller diffraction angles (Fig. 2d). This excludes thermal expansion as the

origin of the electromechanical response of the MAPbI<sub>3</sub> single crystals under applied bias.

### Stability and temporal response of electrostriction

In order to evaluate the strain stability and response time of electrostriction for the MAPbI<sub>3</sub> single crystals, we applied a rectangular-shaped bias pulse with a duration of 60 s and measured the resulting strain with the AFM tip. When the d.c. bias was switched on, the electrostrictive strain appeared immediately and remained unchanged after 60 s (Fig. 3a). The electrostrictive performance was also found to be highly repeatable during 1200 actuation loops under an a.c. applied bias (Supplementary Fig. 3). Therefore, the MAPbI<sub>3</sub> single crystals have stable electrostrictive response under applied field. The quick response of AFM (<0.5 ms, *E*-*t* curve in Fig. 3b) allows us to examine the dynamics of the field-induced electrostrictive deformation. We found that the electrostrictive response time of the MAPbI<sub>3</sub> single crystals is several milliseconds (Fig. 3b). As a result, the electrostrictive strain was fast enough to follow the change of electric field under a.c. bias with a frequency of up to 10 Hz (Fig. 3c). However, when the frequency of a.c. bias is increased to the kilohertz range, the electrostrictive strain cannot follow the change of electric field, and the electrostrictive response is negligible. This was verified using laser interferometer measurement, with results shown in Supplementary Fig. 4.

### Mechanism of electrostriction in MAPbI<sub>3</sub> single crystal

Here we consider two possible reported mechanisms, the intrinsic electrostrictive effect and Maxwell stress effect<sup>13-27</sup>, for the basic observation that the measured strain is proportional to the square of the applied voltage for MAPbI<sub>3</sub> (Equation 1). However, we find that the electrostriction of the MAPbI<sub>3</sub> single crystal cannot be explained by either of them. The intrinsic electrostrictive effect, due to anharmonic displacement of positive ions and negative ions under applied bias, dominates the electrostrictive response of relaxor ferroelectrics, and it induces lattice expansion instead of compression, because the energy required to compress the ionic bonds is

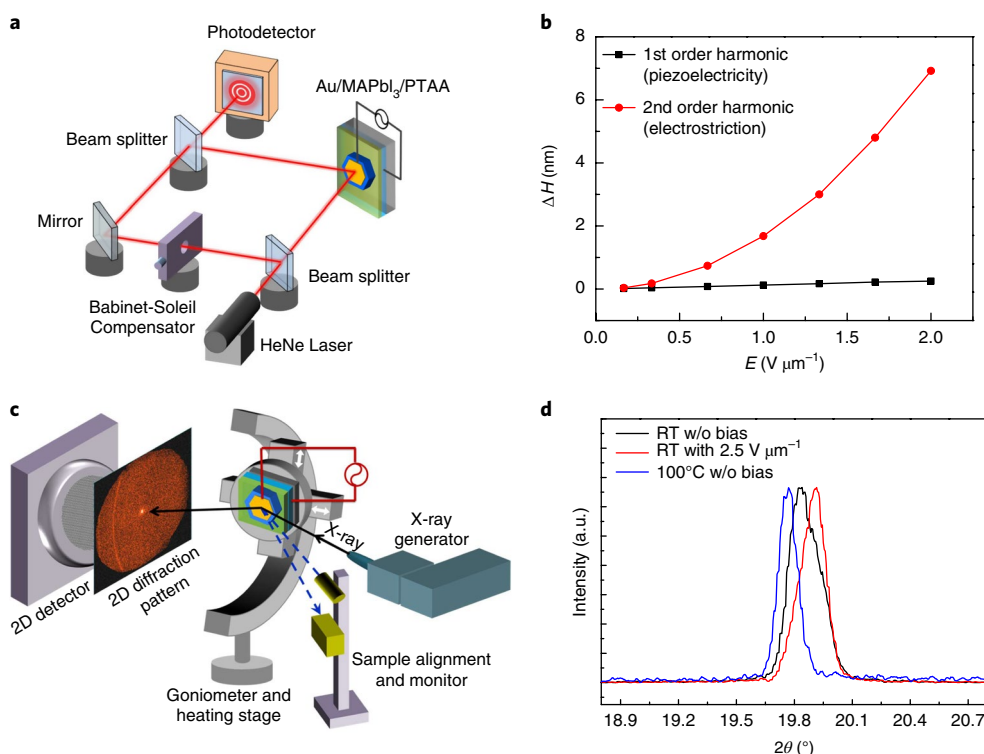


**Fig. 2 | Macroscopic measurement of electrostrictive response for MAPbI<sub>3</sub> single crystal.** **a**, Schematic illustration of Mach-Zehnder interferometer set-up. **b**, Thickness change due to first-order piezoelectricity and second-order electrostriction for a 40 μm MAPbI<sub>3</sub> single crystal under 100 Hz a.c. with different field amplitudes. **c**, Schematic illustration of XRD measurement for MAPbI<sub>3</sub> single crystal under bias. **d**, XRD spectra of MAPbI<sub>3</sub> single crystal under different conditions: pristine, under applied bias and under heating.

generally larger than that to expand the ionic bonds<sup>20,36</sup>. This creates positive strain for relaxor ferroelectrics under bias (as summarized in Table 1), which contradicts the negative strain for MAPbI<sub>3</sub> observed in our study. Moreover, the response time of ion displacement due to bond elongation inside the unit cell is reported to be in the microsecond range<sup>37</sup>, which is orders of magnitude faster than what is measured here. Therefore, the intrinsic electrostrictive effect cannot be the sole origin of the large electrostriction in MAPbI<sub>3</sub>.

Maxwell stress is caused by Coulombic interaction between uncompensated charges (due to imperfect screening) on the electrodes<sup>24</sup>. The strain induced by Maxwell stress ( $S_{\text{Maxwell}}$ ) can be calculated from

$$S_{\text{Maxwell}} = -1/2 \times \epsilon \epsilon_0 (1 + 2\nu) E^2 / Y \quad (2)$$

where  $\epsilon$  is the relative dielectric permittivity,  $\epsilon_0$  is the vacuum dielectric permittivity and  $\nu$  is the Poisson ratio<sup>24</sup>. Using the Young's modulus of 14.8 GPa and the Poisson ratio of 0.33<sup>38</sup>, an  $\epsilon$  value of 1,500,000 is required for MAPbI<sub>3</sub> to generate a strain of 1% under  $3.7 \text{ V } \mu\text{m}^{-1}$ , which is at least four orders of magnitude higher than the reported dielectric permittivity value for MAPbI<sub>3</sub> ( $\epsilon = 30\text{--}70$ )<sup>39,40</sup>. Migration of ions under applied electric field may cause ion accumulation at perovskite-electrode interfaces, which could also induce Maxwell strain. However, we found that accumulated ions at the interface cannot generate such high strain (Supplementary Information Section 6.0). Moreover, the amount of ion accumulation would increase with the bias duration, and a reverse bias is needed to remove the accumulated ions. The stable electrostrictive strain output under bias and hysteresis-free strain-field relation further qualitatively rule out ion accumulation at the interface as the dominating mechanism for the electrostriction. This reveals

that the Maxwell stress effect is probably not significant for the electromechanical response of the MAPbI<sub>3</sub> device.

We further considered the impact of methylammonium cation (MA<sup>+</sup>) ordering, local polar fluctuations and ferroelectric polarization switching under an applied electric field on the electromechanical response. Considering that the calculated energy barrier for structural inversion induced by MA<sup>+</sup> ordering is of the order of 20 meV (Supplementary Information Section 7.0), the MA cation reorientation occurs on the picosecond timescale<sup>41,42</sup>, which does not account for the much slower response observed here. Moreover, when replacing the polar MA<sup>+</sup> with non-polar Cs<sup>+</sup>, we found that CsPbI<sub>3</sub> also demonstrated electrostriction characteristics under applied bias (Supplementary Fig. 7). This excludes a major contribution of MA<sup>+</sup> ordering to the electrostriction of OIHPs. In addition to organic dipoles, local polar fluctuations, such as rotational disordering of I atoms in the PbI<sub>6</sub><sup>4-</sup> octahedra<sup>43</sup> and head-to-head Cs motion coupled to lattice expansion<sup>44</sup>, is also several orders of magnitude faster than the observed electromechanical response of MAPbI<sub>3</sub> reported here. We further investigated the electrostrictive response of cubic MAPbBr<sub>3</sub>, which has centrosymmetric structure and thus is not ferroelectric, and this also demonstrated high electrostrictive strain under applied bias (Supplementary Fig. 8), which excludes a dominant impact of the ferroelectric effect on the electrostriction of OIHPs. The hysteresis-free strain-field relation further verifies that the electrostriction of OIHPs is not related to ferroelectricity.

Considering that the observed millisecond timescale for the electrostrictive response is close to that typically associated with ion/defect migration in OIHPs, we speculate that the observed electrostriction is related to defect formation. Long-range ion migration under electric field cannot change the shape of the material,

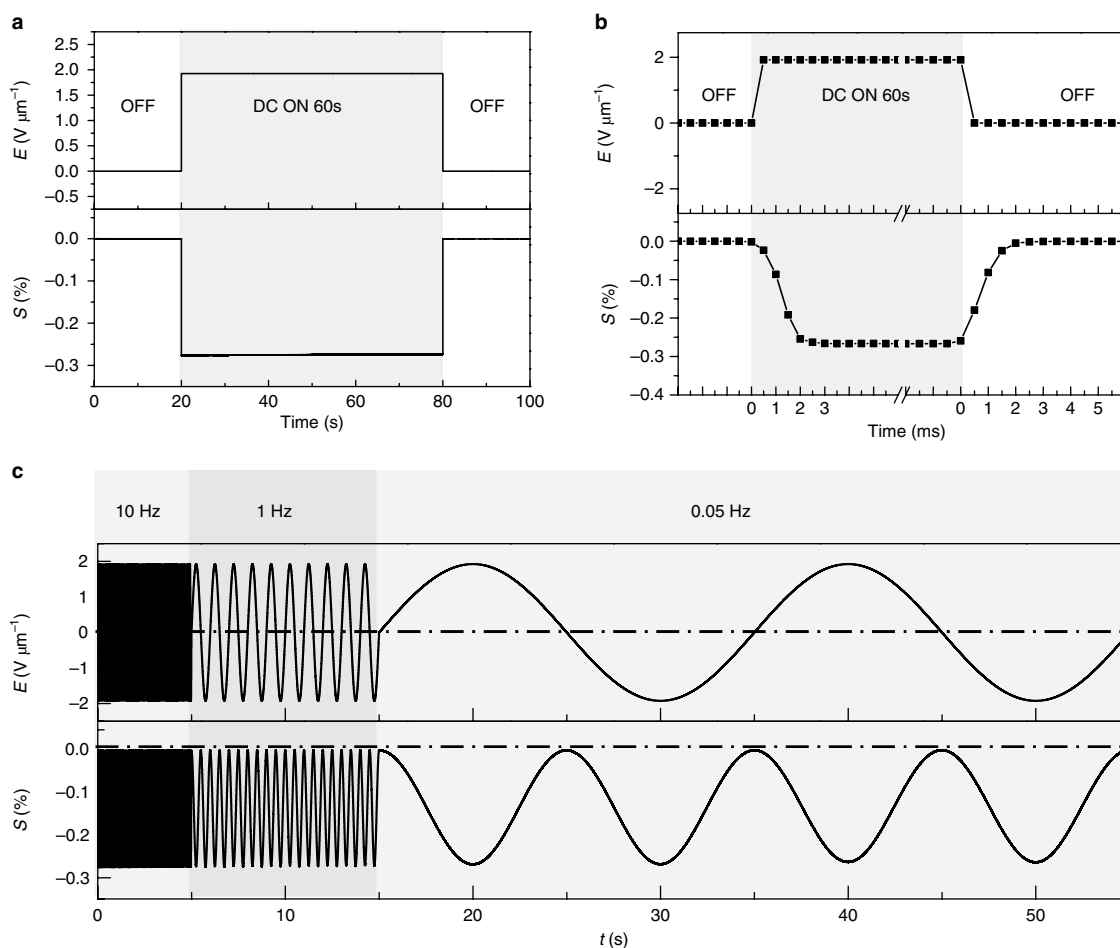


**Fig. 3 | Stability and response timescale of electrostriction.** **a**, Electrostrictive strain of MAPbI<sub>3</sub> single crystal under d.c. bias pulse. **b**, Enlarged *S*-*t* and *E*-*t* curves (*t*, time) when bias was switched on at 20 s and switched off at 80 s. **c**, Electrostrictive responses under different frequencies of applied bias. All electrostrictive responses were measured using AFM.

because ions would only move to a different crystal region without changing the crystal volume or strain. It has been reported that MAPbI<sub>3</sub> has small ionic point defect formation energies<sup>45,46</sup>. We propose that lattice deformation is possibly caused by formation of additional defects, probably iodine Frenkel pairs, under electric field, and that this generates an electromechanical response in OIHPs. Computation (Supplementary Figs. 9–14) shows that the formation of iodine Frenkel defects under electric field could induce a strain of +0.3% along the *a/b* axis and of -0.6% along the *c* axis (Supplementary Fig. 11), comparable to the experimentally measured electrostrictive strain. Upon removing the electric field the starting pristine situation is restored (Supplementary Fig. 11d), due to the attraction and annihilation between the oppositely charged defects. The Arrhenius relation between the electrostrictive response and temperature (Supplementary Fig. 15) and reduction of effective activation energy for ion migration in perovskite with increasing field (Supplementary Fig. 16) provide a connection between electrostriction and defect formation/annihilation, lending support to the proposed mechanism.

## Outlook

Since almost every electronic device either operates under applied electric field or experiences an internal built-in field, which is close to the field of 3.7 V μm<sup>-1</sup> inducing 1% strain, the discovery of electrostriction and its origin may also impact the design and performance of OIHP-based electronic devices, including solar

cells, LEDs, photodetectors and radiation detectors. For perovskite solar cells, we recently found that the presence of remnant lattice strain in OIHP polycrystalline films could accelerate their degradation under illumination<sup>47</sup>. The electrostrictive strain of OIHP polycrystalline films is expected to impact the stability of perovskite solar cells by adding additional strain to perovskite grains. For a typical perovskite solar cell with open-circuit voltage of 1.08–1.15 V and OIHP film thickness of 300–500 nm, the built-in electric field under the maximum power point condition is 0.30–0.65 V μm<sup>-1</sup>. This could generate an electrostrictive strain of about 0.01–0.03% at the maximum power point condition based on an electrostrictive coefficient of -730 nm<sup>2</sup>V<sup>-2</sup>. We have recently reported that polycrystalline MAPbI<sub>3</sub> films have tensile strain (~0.47%) in the in-plane direction, which is formed in the cooling process due to mismatched thermal expansion of MAPbI<sub>3</sub> with the substrate<sup>47</sup>. In this case, the electrostriction sets a new stable state with a larger lattice along the in-plane direction, which thus reduces the tensile strain caused by thermal annealing and improves the device stability. We also find that some perovskite films (such as FA<sub>0.85</sub>MA<sub>0.15</sub>Pb(I<sub>0.85</sub>Br<sub>0.15</sub>)<sub>3</sub>) have much less or no annealing-induced remnant lattice strain. Therefore, electrostrictive strain could accelerate device degradation, though the impact will not be significant due to the small electrostrictive strain induced. Similarly, the electrostrictive strain changes the ion migration rate in OIHPs, and thus will also impact the stability of LEDs and detectors. The field-induced defect generation also sets a lower limit of carrier concentration in hybrid

perovskites. Since a high dark conductivity is crucial for detectors such as radiation detectors, strategies to mitigate the electrostriction effect would be needed to design single-photon detectors using OHIPs. The electron–phonon interaction has been reported to be crucial in determining several unique properties of OHIPs<sup>48</sup>, such as long hot-carrier relaxation lifetime in OHIP materials<sup>49</sup>. The electrostrictive strain is thus expected to have an influence on the carrier mobility and hot-carrier relaxation lifetime, which should be further studied in the future. Finally, the large electrostriction of MAPbI<sub>3</sub> crystals could have a broad range of potential applications in, for example, actuators, sonar transducers and integrated micro-electromechanical systems.

### Online content

Any methods, additional references, Nature Research reporting summaries, source data, statements of data availability and associated accession codes are available at <https://doi.org/10.1038/s41563-018-0170-x>.

Received: 10 August 2017; Accepted: 16 August 2018;

Published online: 24 September 2018

### References

- Yang, W. S. et al. Iodide management in formamidinium-lead-halide-based perovskite layers for efficient solar cells. *Science* **356**, 1376–1379 (2017).
- NREL Best research-cell efficiencies. <https://www.nrel.gov/pv/assets/images/efficiency-chart-20180716.jpg> (accessed 16 July 2018).
- Fang, Y. & Huang, J. Resolving weak light of sub-picowatt per square centimeter by hybrid perovskite photodetectors enabled by noise reduction. *Adv. Mater.* **27**, 2804–2810 (2015).
- Shen, L. et al. A self-powered, sub-nanosecond-response solution-processed hybrid perovskite photodetector for time-resolved photoluminescence-lifetime detection. *Adv. Mater.* **28**, 10794–10800 (2016).
- Fang, Y., Dong, Q., Shao, Y., Yuan, Y. & Huang, J. Highly narrowband perovskite single-crystal photodetectors enabled by surface-charge recombination. *Nat. Photon.* **9**, 679–686 (2015).
- Wei, W. et al. Monolithic integration of hybrid perovskite single crystals with heterogeneous substrate for highly sensitive X-ray imaging. *Nat. Photon.* **11**, 315–321 (2017).
- Wei, H. et al. Dopant compensation in alloyed CH<sub>3</sub>NH<sub>3</sub>PbBr<sub>3-x</sub>Cl<sub>x</sub> perovskite single crystals for gamma-ray spectroscopy. *Nat. Mater.* **16**, 826–833 (2017).
- Sutherland, B. R. & Sargent, E. H. Perovskite photonic sources. *Nat. Photon.* **10**, 295–302 (2016).
- Xiao, Z. G. et al. Efficient perovskite light-emitting diodes featuring nanometre-sized crystallites. *Nat. Photon.* **11**, 108–115 (2017).
- Gautschi, G. *Piezoelectric Sensors* (Springer, New York, 2002).
- Wang, X., Song, J., Liu, J. & Wang, Z. L. Direct-current nanogenerator driven by ultrasonic waves. *Science* **316**, 102–105 (2007).
- Uchino, K. *Piezoelectric Actuators and Ultrasonic Motors* (Springer, New York, 1997).
- Bobnar, V. et al. Electrostrictive effect in lead-free relaxor K<sub>0.5</sub>Na<sub>0.5</sub>NbO<sub>3</sub>–SrTiO<sub>3</sub> ceramic system. *J. Appl. Phys.* **98**, 024113–024113 (2005).
- Wang, F. F., Jin, C. C., Yao, Q. R. & Shi, W. Z. Large electrostrictive effect in ternary Bi<sub>0.5</sub>Na<sub>0.5</sub>TiO<sub>3</sub>-based solid solutions. *J. Appl. Phys.* **114**, 027004 (2013).
- Li, F., Jin, L. & Guo, R. High electrostrictive coefficient Q<sub>33</sub> in lead-free Ba(Zr<sub>0.2</sub>Ti<sub>0.8</sub>)O<sub>3-x</sub>(Ba<sub>0.7</sub>Ca<sub>0.3</sub>)TiO<sub>3</sub> piezoelectric ceramics. *Appl. Phys. Lett.* **105**, 232903 (2014).
- Park, S. E. & Shrout, T. R. Ultrahigh strain and piezoelectric behavior in relaxor based ferroelectric single crystals. *J. Appl. Phys.* **82**, 1804–1811 (1997).
- Li, F., Jin, L., Xu, Z., Wang, D. & Zhang, S. Electrostrictive effect in Pb(Mg<sub>1/3</sub>Nb<sub>2/3</sub>)O<sub>3-x</sub>PbTiO<sub>3</sub> crystals. *Appl. Phys. Lett.* **102**, 152910 (2013).
- Li, F., Xu, Z. & Zhang, S. The effect of polar nanoregions on electromechanical properties of relaxor-PbTiO<sub>3</sub> crystals: extracting from electric-field-induced polarization and strain behaviors. *Appl. Phys. Lett.* **105**, 122904 (2014).
- Baek, S. et al. Giant piezoelectricity on Si for hyperactive MEMS. *Science* **334**, 958–961 (2011).
- Li, F., Jin, L., Xu, Z. & Zhang, S. Electrostrictive effect in ferroelectrics: an alternative approach to improve piezoelectricity. *Appl. Phys. Rev.* **1**, 011103 (2014).
- Zhang, Q. M., Bharti, V. & Zhao, X. Giant electrostriction and relaxor ferroelectric behavior in electron-irradiated poly(vinylidene fluoride-trifluoroethylene) copolymer. *Science* **280**, 2101–2104 (1998).
- Xu, H. S. et al. Ferroelectric and electromechanical properties of poly(vinylidene-fluoride-trifluoroethylene-chlorotrifluoroethylene) terpolymer. *Appl. Phys. Lett.* **78**, 2360–2362 (2001).
- Bauer, F., Fousson, E. & Zhang, Q. M. Recent advances in highly electrostrictive P(VDF-TrFE-CFE) terpolymers. *IEEE Trans. Dielectr. Electr. Insul.* **13**, 1149–1154 (2006).
- Zhang, Q. M. et al. An all-organic composite actuator material with a high dielectric constant. *Nature* **419**, 284–287 (2002).
- Huang, C. & Zhang, Q. Enhanced dielectric and electromechanical responses in high dielectric constant all-polymer percolative composites. *Adv. Funct. Mater.* **14**, 501–506 (2004).
- Javadi, A., Xiao, Y., Xu, W. & Gong, S. Chemically modified graphene/P(VDF-TrFE-CFE) electroactive polymer nanocomposites with superior electromechanical performance. *J. Mater. Chem.* **22**, 830–834 (2012).
- Le, M. Q. et al. All-organic electrostrictive polymer composites with low driving electrical voltages for micro-fluidic pump applications. *Sci. Rep.* **5**, 11814 (2015).
- Chen, Z. et al. Single crystal perovskite solar cells with broadened light-harvesting spectrum. *Nat. Commun.* **8**, 1890 (2017).
- Dong, Q. et al. Lateral-structure single-crystal hybrid perovskite solar cells via piezoelectric poling. *Adv. Mater.* **28**, 2816–2821 (2016).
- Strelcov, E. et al. CH<sub>3</sub>NH<sub>3</sub>PbI<sub>3</sub> perovskites: ferroelasticity revealed. *Sci. Adv.* **3**, e1602165 (2017).
- Mirfakhrai, T., Madden, J. D. W. & Baughman, R. H. Polymer artificial muscles. *Mater. Today* **10**, 30–38 (2007).
- Cheng, C., Weissmüller, J. & Ngan, A. H. W. Fast and reversible actuation of metallic muscles composed of nickel nanowire-forest. *Adv. Mater.* **28**, 5315–5321 (2016).
- Weissmüller, J. et al. Charge-induced reversible strain in a metal. *Science* **300**, 312–315 (2003).
- Baughman, R. H. Playing nature's game with artificial muscles. *Science* **308**, 63–65 (2005).
- Liu, S., Zheng, F., Grinberg, I. & Rappe, A. M. Photoferroelectric and photopiezoelectric properties of organometal halide perovskites. *J. Phys. Chem. Lett.* **7**, 1460–1465 (2016).
- Uchino, K. *Ferroelectric Devices* (Taylor and Francis, Boca Raton, 2010).
- Damjanovic, D. & Newnham, R. Electrostrictive and piezoelectric materials for actuator applications. *J. Intell. Mater. Syst. Struct.* **3**, 190–208 (1992).
- Feng, J. Mechanical properties of hybrid organic–inorganic CH<sub>3</sub>NH<sub>3</sub>BX<sub>3</sub> (B = Sn, Pb; X = Br, I) perovskites for solar cell absorbers. *APL Mater.* **2**, 081801 (2014).
- Lin, Q. Q., Armin, A., Nagiri, R. C. R., Burn, P. L. & Meredith, P. Electro-optics of perovskite solar cells. *Nat. Photon.* **9**, 106–112 (2015).
- Juarez-Perez, E. J. et al. Photoinduced giant dielectric constant in lead halide perovskite solar cells. *J. Phys. Chem. Lett.* **5**, 2390–2394 (2014).
- Bakulin, A. A. et al. Real-time observation of organic cation reorientation in methylammonium lead iodide perovskites. *J. Phys. Chem. Lett.* **6**, 3663–3669 (2015).
- Quarti, C., Mosconi, E. & De Angelis, F. Interplay of orientational order and electronic structure in methylammonium lead iodide: implications for solar cell operation. *Chem. Mater.* **26**, 6557–6569 (2014).
- Wu, X. et al. Light-induced picosecond rotational disordering of the inorganic sublattice in hybrid perovskites. *Sci. Adv.* **3**, e1602388 (2017).
- Yaffe, O. et al. Local polar fluctuations in lead halide perovskite crystals. *Phys. Rev. Lett.* **118**, 136001 (2017).
- Walsh, A., Scanlon, D. O., Chen, S., Gong, X. G. & Wei, S.-H. Self-regulation mechanism for charged point defects in hybrid halide perovskites. *Angew. Chem.* **127**, 1811–1814 (2015).
- Yin, W.-J., Shi, T. & Yan, Y. Unusual defect physics in CH<sub>3</sub>NH<sub>3</sub>PbI<sub>3</sub> perovskite solar cell absorber. *Appl. Phys. Lett.* **104**, 063903 (2014).
- Zhao, J. et al. Strained hybrid perovskite thin films and their impact on the intrinsic stability of perovskite solar cells. *Sci. Adv.* **3**, eao5616 (2017).
- Miyata, K. et al. Large polarons in lead halide perovskites. *Sci. Adv.* **3**, e1701217 (2017).
- Zhu, H. et al. Screening in crystalline liquids protects energetic carriers in hybrid perovskites. *Science* **353**, 1409–1413 (2016).

### Acknowledgements

This work is financially supported by the Office of Naval Research under award N00014-17-1-2727, the Department of Energy (DOE) under award DE-EE0006709 and the National Science Foundation (NSF) under awards DMR-1505535 and DMR-1420645. E.M. and F.D.A. acknowledge the project PERSEO—'Perovskite-based Solar cells: towards high Efficiency and long-term stability' (Bando PRIN 2015—Italian Ministry of University and Scientific Research (MIUR) Decreto Direttoriale 4 November 2015 no. 2488, project no. 20155LECAJ) for funding.

**Author contributions**

J.H., B.C. and Q.D. conceived the idea. B.C. designed the experiments. T.L. and A.G. conducted the AFM measurements. Q.D., Z.C. and Y.L. grew the single crystal. E.M. and F.D.A. conducted the computational simulations. J.S. and S.D. performed Mach-Zehnder interferometer measurements. Y.D. carried out the XRD measurement. B.C., F.D.A. and J.H. wrote the paper, and all authors reviewed the paper.

**Competing interests**

The authors declare no competing interests.

**Additional information**

**Supplementary information** is available for this paper at <https://doi.org/10.1038/s41563-018-0170-x>.

**Reprints and permissions information** is available at [www.nature.com/reprints](http://www.nature.com/reprints).

**Correspondence and requests for materials** should be addressed to F.D.A. or J.H.

**Publisher's note:** Springer Nature remains neutral with regard to jurisdictional claims in published maps and institutional affiliations.

## Methods

**Device fabrication.** MAPbI<sub>3</sub> single crystals with 40 μm thickness were grown on PTAA-coated ITO-glass by a hydrophobic-interface-confined method; more details can be found in our previous paper<sup>26</sup>. In brief, 1.5 M MAPbI<sub>3</sub> precursor in  $\gamma$ -butyrolactone was injected into two PTAA-coated ITO-glass substrates. Subsequently, the samples were placed on a hotplate at a temperature of 100 °C for 1 h, followed by 110 °C for 1 h and 120 °C for 12 h to further promote the growth of the single crystal. The two ITO-glass substrates were separated and left on the hotplate and the temperature slowly cooled to room temperature. Finally, 50 nm Au was thermally evaporated on top of the MAPbI<sub>3</sub> single crystal.

**Characterizing electrostriction with AFM.** The detection of sample oscillation triggered by an alternating electric field was realized using a commercial atomic force microscope (MFP-3D-BIO, Asylum Research). All of the measurements were conducted in a closed cell with continuous flow of dry nitrogen. During the measurement, an electric bias was supplied to a Pt-Ir-coated conductive probe (PPP-EFM, NANOSENSORS), which was in contact with the gold electrode on top of the MAPbI<sub>3</sub> crystal surface. The contact force was maintained at about 60 nN to 70 nN to ensure a good electronic contact between tip and sample. Cantilever stiffness and sensitivity were calibrated before each measurement. The bottom side of the MAPbI<sub>3</sub> crystal was grounded through the ITO substrate. According to the electrostriction behaviour of MAPbI<sub>3</sub>, the a.c. bias concomitantly initiates mechanical oscillations of the crystal, which were detected and displayed as periodic deflection signals of the cantilever. The oscillating height change of the sample was recorded over time.

**Measuring electromechanical strain with optical interferometry.** The electrostrictive response of the crystals was measured using a Mach-Zehnder interferometer, consisting of a 6 mW He-Ne laser with a beam diameter of approximately 1 mm, a silicon photodetector, beam splitters and mirrors, one of which was deposited on top of the crystal (see Fig. 2a). The laser interferometer output was measured with a lock-in amplifier, which can distinguish the signal with frequency up to 100 kHz and thus give a time resolution of 10 μs. The amplitude of the thickness change at each frequency was calculated from the amplitude of the intensity modulation  $\Delta I(f, 2f)/I_{\text{avg}}$ , the He-Ne emission wavelength  $\lambda = 633$  nm and the crystal thickness  $d$  according to the expression  $\Delta d(f, 2f) = 2^{3/2} \pi \lambda [\Delta I(f, 2f)/I_{\text{avg}}]$  (Supplementary Information Section 1.0).

**Activation energy determination.** The activation energy for ion migration under different fields was determined according to ref. 47, and is reproduced here for completeness. Specifically, the conductivities of the ITO-PTAA-MAPbI<sub>3</sub>-Au device were measured with a Lakeshore Probe Station under a vacuum of 10<sup>-5</sup> Pa. The temperature was regulated by a heater and injected liquid nitrogen. The current measurement was carried out with a Keithley 2400 under different fields at different temperatures. The temperature was first reduced to 120 K and stabilized for 30 min, then slowly increased to 330 K with a step of 10 K. The current was measured after temperature was stabilized for 10 min.

**Structure determination with XRD.** The XRD structure was obtained using a Bruker-AXS D8 Discover diffractometer with a Vantec-500 area detector and Cu K-alpha radiation (wavelength 1.54 Å). The X-ray source, with a beam size of 1 mm, was aligned on the Au-coated MAPbI<sub>3</sub> single-crystal surface.

**Computational details.** The tetragonal MAPbI<sub>3</sub> perovskite was simulated with a 1 × 1 × 1 unit cell containing four formula units (48 atoms) and with a larger 2 × 2 × 2 supercell (384 atoms). All calculations have been carried out using the Quantum Espresso program package along with the Perdew-Burke-Ernzerhof (PBE) functional. Electron-ion interactions were described by scalar relativistic ultrasoft pseudopotentials with electrons from O, N and C 2s2p, H 1s, Pb 6s6p5d and I 5s5p electrons explicitly included in the calculations. A 4 × 4 × 4  $k$ -point mesh for sampling the Brillouin zone was used for the 1 × 1 × 1 cell; see convergence tests and benchmarks in Supplementary Information. Spin-orbit coupling was included to evaluate its effect on the stability of Frenkel defects. Calculations employing the experimental cell parameters were performed using plane-wave cutoffs of 25 and 200 Ry for expansion of the wavefunction and density, respectively, while for variable cell calculations and for calculations in the presence of the field 50 and 400 Ry cutoffs are used, including dispersion interactions with the D2 approach. A homogeneous finite electric field, described through the modern theory of polarization, is applied as implemented in Quantum Espresso. Convergence thresholds on the energy and forces were investigated up to 10<sup>-7</sup> Ry and 10<sup>-4</sup> Ry/a.u., respectively.

## Data availability

The authors declare that all relevant data supporting the findings of this study are available within the paper and its Supplementary Information.